Finite element discretization and Newton-multigrid solution techniques for the log-conformation reformulation (LCR) of viscoelastic flow problems ⋆

H. Damanik [a,*], J. Hron [b], A. Ouazzi [a], S. Turek [a]

[a] *Institut für Angewante Mathematik, TU Dortmund, Germany*

[b] *Institute of Mathematics, Charles University, Czech Republic*

Abstract

We present special numerical techniques for viscoelastic fluid flow utilizing a fully coupled monolithic multigrid finite element approach with consistent edge-oriented stabilization technique. The governing equations arise from the Navier-Stokes equations for the Oldroyd-B type of fluid with the help of the log-conformation reformulation ("Kupferman's trick") to allow a wide range of Weissenberg numbers. The resulting nonlinear system consists of 6 variables for velocity, pressure and the logarithm of the conformation stress tensor in 2D. The system is discretized in time by using a fully implicit second order accurate time integrator. In each time step, we have to solve a discretized system in space employing the high order finite element pair Q_2/P_1. We utilize the discrete damped Newton method with divided differences for handling the Jacobian, and apply a geometrical multigrid solver with a special Vanka smoother to handle the linear subproblems. Local refinement can be assigned at regions of interest to reduce the computational efforts. The presented methodology is implemented and validated for several well-known benchmark problems.

Key words: Monolithic multigrid, FEM, Non-Newtonian, Viscoelastic flow, Oldroyd-B, Log-conformation reformulation (LCR)

⋆ This research was supported by the Graduate School of Production Engineering and Logistics and by the German Research Foundation (DFG) through the collaborative research center SFB/TR TRR 30 and through the grants TU 102/11-3 (FOR493) and TU 102/21-1

* Corresponding author.

Email addresses: hdamanik@math.tu-dortmund.de (H. Damanik), hron@karlin.mff.cuni.cz (J. Hron), ouazzi@math.tu-dortmund.de (A. Ouazzi), ture@featflow.de (S. Turek).

1 INTRODUCTION

The term non-Newtonian fluid is still open to interpretation. It is often mentioned together with the term viscoelasticity because it provides not only the properties of viscous fluids but also additional elastic properties. For quasi-Newtonian fluids, the stress depends only on the deformation rate, while for elastic fluid it depends additionally on the elastic stress that has its own constitutive law. The characterization of viscoelastic fluids is rather a mixture of both idealized properties. The fact that this kind of fluid combines two different properties manifests itself in a wide range of physical phenomena depending on the relaxation time of the fluid, Λ, which is represented by the non-dimensional Weissenberg number, $We = \frac{\Lambda v_c}{l_c}$, inside the constitutive material law. By v_c and l_c we refer to the characteristic velocity and length. In this study, we focus on Oldroyd-B type of constitutive laws which uses a macroscopic approach to model the viscoelastic fluid. Apart from its simplicity this type of fluid has been the most difficult one to treat numerically. Many numerical schemes break down at $We \sim 1$ which is the entry point to critical elastic flow. The failure of numerics to give solutions at critical elastic flow numbers is due to the inability of the model itself to capture the microscopic physical behavior such as coil-stretch transition [4] so that as a consequence current numerical techniques are often inadequate to deal with this problem [28]. Furthermore in [41] it is said that the smoothness of viscoelastic stresses should be expected to deteriorate with increasing elastic property. Steep stress gradients which grow exponentially occur behind a stagnation point inside the domain which leads to further numerical instabilities. Therefore, the CFD community has been trying to solve this problem by updating numerical techniques so far. In a recent study of Fattal and Kupferman [18], however, they change the main variable in a way so that the new variable is able to capture this exponential property. Their reformulation which uses a logarithmic transformation (LCR) is able to maintain numerical stability at higher We number than before and will be the basis of our numerical approach. Several corresponding articles [1,12,26,38] have successfully implemented LCR in different ways. In contrast to those previous studies, we present a new monolithic Newton-multigrid approach in a fully coupled frame work with consistent edge-oriented FEM stabilization technique which in an implicit finite element frame can work together with local refinement utilizing hanging nodes in a proper way to provide highly accurate results.

This paper is structured as follows: In the following section 2, we briefly formulate the set of equations to solve. From there on, in section 3, we discretize the flow problem in two space dimensions by utilizing the Q_2P_1 finite element pair in a standard FEM approach, after applying a standard implicit one-step time-stepping scheme in the nonstationary case. And then, in section 4, we treat the resulting discrete problems in a fully coupled monolithic way for

$(\mathbf{u}, p, \boldsymbol{\psi})$ by utilizing outer Newton iterations and inner multigrid solvers with special smoothers such that we maintain high efficiency and robustness rates, even on general meshes allowing the assignment of hanging nodes. In the numerical section 5, we consider first a nonstationary cavity problem and then show direct steady calculations for flow around cylinder and for the well-known 4 to 1 contraction configuration.

2 PROBLEM FORMULATION

A general material law for viscoelastic flow is given below following Oldroyd [36, 44]

$$\mathbf{T} + \Lambda \frac{\delta_a \mathbf{T}}{\delta t} = 2\eta_0 \left(\mathbf{D} + \Lambda_r \frac{\delta_a \mathbf{D}}{\delta t} \right) \tag{1}$$

where $\mathbf{T}, \mathbf{D}, \eta_0, \Lambda, \Lambda_r$ are the total stress, symmetric part of velocity gradient, total viscosity, relaxation time, and retardation time. The total viscosity is the well-known zero-shear viscosity which can be found in fluid mechanics books. In this study we prefer to calling it total viscosity since it is the sum of Newtonian viscosity (η_s) and elastic viscosity (η_p). We like to note that the model from Oldroyd cames from the Jeffreys model of viscoelasticity which consists of a series of dashpot and Voigt-Kelvin elements. This means that the deformation of such a model is unbounded in time and always viscous by design [27]. Depending on how we choose the parameters a and Λ_r, we may recover a wide range of viscoelastic models such as Maxwell A or B, Oldroyd A or B, Jeffreys and many more. The stress tensor $\mathbf{T}$ consists of two parts, that are the elastic component, $\boldsymbol{\sigma}$, and the purely viscous component, $2\eta_0 \frac{\Lambda_r}{\Lambda} \mathbf{D}$, where each of them contributes to the total stress, $\mathbf{T} = 2\eta_0 \frac{\Lambda_r}{\Lambda} \mathbf{D} + \boldsymbol{\sigma}$. By replacing $\mathbf{T}$ in equation (1) with $\boldsymbol{\sigma}$, we end up with the following equation:

$$\Lambda \frac{\delta_a \boldsymbol{\sigma}}{\delta t} - 2\eta_p \mathbf{D} + \boldsymbol{\sigma} = 0 \quad \text{with} \quad \eta_p = \eta_0 \left(1 - \frac{\Lambda_r}{\Lambda} \right). \tag{2}$$

Furthermore the extended material time derivative, $\frac{\delta_a \boldsymbol{\sigma}}{\delta t}$, is defined as follows:

$$\frac{\delta_a \boldsymbol{\sigma}}{\delta t} = \frac{D\boldsymbol{\sigma}}{Dt} + \underbrace{\frac{1-a}{2} \left(\nabla \mathbf{u}^T . \boldsymbol{\sigma} + \boldsymbol{\sigma} . \nabla \mathbf{u} \right) + \frac{1+a}{2} \left(-\nabla \mathbf{u} . \boldsymbol{\sigma} - \boldsymbol{\sigma} . \nabla \mathbf{u}^T \right)}_{stretching}. \tag{3}$$

Note that the extended material time derivative refers to the Lagrangian or material time derivative $\frac{D(\cdot)}{Dt}$ plus additional stretching term which is written in a way that we may choose the upper- or lower-convected time derivative. Furthermore, we decompose the gradient of velocity into a symmetric ($\mathbf{D}$) and a skew-symmetric ($\mathbf{W}$) part,

$$\nabla \mathbf{u} = \mathbf{D} + \mathbf{W} \quad \text{with} \quad \mathbf{D} = \frac{1}{2}(\nabla \mathbf{u} + \nabla \mathbf{u}^T) \quad \text{and} \quad \mathbf{W} = \frac{1}{2}(\nabla \mathbf{u} - \nabla \mathbf{u}^T) \tag{4}$$

and rewrite the extended material time derivative as:

$$\frac{\delta_a \boldsymbol{\sigma}}{\delta t} = \frac{D\boldsymbol{\sigma}}{Dt} - \mathbf{W}.\boldsymbol{\sigma} + \boldsymbol{\sigma}.\mathbf{W} - a\ \mathbf{D}.\boldsymbol{\sigma} - a\ \boldsymbol{\sigma}.\mathbf{D} \tag{5}$$

The last two terms are often denoted as Johnson-Segalman model for which we will focus on $a = 1$ so that it reduces to the well-known Oldroyd-B model. For simulation purpose, we denote $\eta_0 = 1$ and recast the equation introducing $\beta = \frac{\Lambda_r}{\Lambda}$ as the amount of solvent contribution:

$$\Lambda \left(\frac{\partial \boldsymbol{\sigma}}{\partial t} + (\mathbf{u}.\nabla)\sigma - \nabla\mathbf{u}.\boldsymbol{\sigma} - \boldsymbol{\sigma}.\nabla\mathbf{u}^T \right) + 2\eta_0 \left(\beta - 1\right) \mathbf{D} + \boldsymbol{\sigma} = 0. \tag{6}$$

From this point, the computational rheologist introduces the conformation tensor $\boldsymbol{\tau}$, which is positive definite [25]

$$\boldsymbol{\sigma} = \frac{\eta_p}{\Lambda}(\boldsymbol{\tau} - \mathbf{I}), \tag{7}$$

to replace the stress variable in (6). With the help of the following identity for $a = 1, \frac{\delta_a \mathbf{I}}{\delta t} = 2\mathbf{D}$, we may rewrite the Oldroyd-B model in terms of the conformation tensor $\boldsymbol{\tau}$:

$$\frac{\partial \boldsymbol{\tau}}{\partial t} + \overbrace{(\mathbf{u}.\nabla)\boldsymbol{\tau}}^{convection} \underbrace{-\nabla\mathbf{u}.\boldsymbol{\tau} - \boldsymbol{\tau}.\nabla\mathbf{u}^T}_{stretching} + \frac{1}{\Lambda}(\boldsymbol{\tau} - \mathbf{I}) = 0. \tag{8}$$

It is worth to note that this tensor also has an integral form with exponential expression in it

$$\boldsymbol{\tau}(t) = \int_{\infty}^{t} \frac{1}{\Lambda} exp\left(\frac{-(t-s)}{\Lambda} \right) F(s,t)F(s,t)^T ds \tag{9}$$

where $F(s,t)$ is the relative deformation gradient [31, 37].

This constitutive equation is then coupled with the well-known flow model which is governed by the Navier-Stokes equations arising from the classical equation of continuity

$$\nabla \cdot \mathbf{u} = 0, \tag{10}$$

and the equations of motion with the body force term which can be written as

$$\rho \frac{\partial \mathbf{u}}{\partial t} + \rho(\mathbf{u} \cdot \nabla)\mathbf{u} = -\nabla p + \nabla \cdot \mathbf{T}. \tag{11}$$

The coupling is via the divergence of the total stress, that means

$$\nabla \cdot \mathbf{T} = 2\eta_s \nabla \cdot \nabla\mathbf{u} + \frac{\eta_p}{\Lambda} \nabla \cdot \boldsymbol{\tau} \tag{12}$$

where $\mathbf{u}, t, p, \rho$ are the velocity vector, time, pressure and density. In this study, we will use an equal contribution of solvent and polymeric viscosities ($\beta = 0.5$)

for the driven cavity problem, while for the flow around cylinder and the 4 to 1 contraction problem we use $\beta = 0.59$ and $\beta = \frac{1}{9}$ respectively. To sum up all equations (11, 10, and 8), we rewrite the set of differential equations as follows:

$$\begin{cases} \rho\frac{\partial \mathbf{u}}{\partial t} + \rho(\mathbf{u}\cdot\nabla)\mathbf{u} = -\nabla p + 2\eta_s\Delta\mathbf{u} + \frac{\eta_p}{\Lambda}\nabla\cdot\boldsymbol{\tau} \\ \nabla\cdot\mathbf{u} = 0 \\ \frac{\partial \boldsymbol{\tau}}{\partial t} + (\mathbf{u}\cdot\nabla)\boldsymbol{\tau} - \nabla\mathbf{u}\cdot\boldsymbol{\tau} - \boldsymbol{\tau}\cdot\nabla\mathbf{u}^T + \frac{1}{\Lambda}(\boldsymbol{\tau} - \mathbf{I}) = 0 \end{cases} \tag{13}$$

This set of equations faces numerical difficulties at critical elastic flow numbers which is often attributed to the loss of positivity of the conformation tensor during numerical computation. In [26] it is shown for 1D problems that the convection part is not able to balance the exponential growth of the stress. By introducing a new logarithmic variable, the positive property of the conformation tensor is preserved by design. We will shortly revisit how the reformulation is done in [17] from our viewpoint. Inside their work, the conformation tensor is replaced by a new variable $\boldsymbol{\psi} = R\ log(\boldsymbol{\tau})R^T$ through eigenvalue computations. The reformulation starts with rotating the conformation tensor $\boldsymbol{\tau}$ into its main principle axis (diagonalization process)

$$R^T\boldsymbol{\tau}R = diag(\lambda_1, \lambda_2) \tag{14}$$

with R being an orthogonal matrix. The goal is to design a symmetric matrix $\mathbf{B}$ which commutes with the conformation tensor, a pure rotation matrix $\boldsymbol{\Omega}$ (anti-symmetric matrix) and an additional 'dummy part' matrix $\mathbf{N}\boldsymbol{\tau}^{-1}$ where $\mathbf{N}$ is an anti-symmetric matrix in terms of the velocity gradient

$$\nabla\mathbf{u} = \mathbf{B} + \boldsymbol{\Omega} + \mathbf{N}\boldsymbol{\tau}^{-1}. \tag{15}$$

Here, the matrix $\mathbf{N}$ and $\boldsymbol{\Omega}$ are in pure rotational form, see [17]. Note the small different decomposition with the one from equation (4) where the symmetric matrix $\mathbf{D}$ and the skew-symmetric matrix $\mathbf{W}$ are not subtracted by the component from the 'dummy part'. This special decomposition is in fact the core technique of this reformulation. The challenging task is again how to express those matrices in terms of the velocity gradient. Here, the idea is to take the rotation matrix R and apply it to all components of the velocity gradient. Consequently we obtain

$$R^T\nabla\mathbf{u}R = R^T\mathbf{B}R + R^T\boldsymbol{\Omega}R + R^T\mathbf{N}\boldsymbol{\tau}^{-1}R. \tag{16}$$

By doing so, we have the possibility to easily define $\mathbf{B}$ to be commutable with $\boldsymbol{\tau}$. From equation (14) it is easy to see that $R^T\mathbf{B}R$ in (16) has to be a diagonal matrix in order that it commutes with $R^T\boldsymbol{\tau}R$. A good candidate for this purpose is that we set this term to be equal as the diagonal part of the rotated velocity gradient, $R^T\mathbf{B}R = diag(R^T\nabla\mathbf{u}R)$. So, let $k_{ij} = R^T\nabla\mathbf{u}R$

be the rotated velocity gradient and define $R^T\mathbf{B}R = k_{ii}$. Now since we have an explicit matrix $\mathbf{B}$ in terms of the velocity gradient, we may easily define the rest matrices $(\mathbf{\Omega}, \mathbf{N})$. The second term of equation (16), $R^T\mathbf{\Omega}R$, is in pure rotational form and the last term, $R^T\mathbf{N}\boldsymbol{\tau}^{-1}R$, by the help of equation (14), is also in pure rotational form. Now, we can extract two linear equations from the off-diagonal terms of equation (16) and express the last two matrices $(\mathbf{\Omega}, \mathbf{N})$ in terms of the velocity gradient as shown in [17].

In the end, the matrix $\mathbf{B}$ is not purely extensional, but it commutes with the conformation tensor $\boldsymbol{\tau}$ since it is designed so that both $\mathbf{B}$ and $\boldsymbol{\tau}$ should be in the same plane. By inserting the decomposition (15) into (13) the constitutive law transforms into (17)

$$\frac{\partial \boldsymbol{\tau}}{\partial t} + (\mathbf{u}.\nabla)\boldsymbol{\tau} - (\mathbf{\Omega}.\boldsymbol{\tau} - \boldsymbol{\tau}.\mathbf{\Omega}) + 2\mathbf{B}.\boldsymbol{\tau} = \frac{1}{\Lambda}(\mathbf{I} - \boldsymbol{\tau}). \tag{17}$$

Finally, by replacing the conformation tensor with the new variable $\boldsymbol{\psi} = log(\boldsymbol{\tau})$, the Oldroyd-B model evolves to

$$\frac{\partial \boldsymbol{\psi}}{\partial t} + (\mathbf{u}.\nabla)\boldsymbol{\psi} - (\mathbf{\Omega}.\boldsymbol{\psi} - \boldsymbol{\psi}.\mathbf{\Omega}) + 2\mathbf{B} = \frac{1}{\Lambda}\ (e^{-}\boldsymbol{\psi} - \mathbf{I}). \tag{18}$$

Hence the new set of equations to be solved can be finally rewritten as follows:

$$\begin{cases} \rho\frac{\partial \mathbf{u}}{\partial t} + \rho(\nabla \mathbf{u})\mathbf{u} = -\nabla p + 2\eta_s \Delta \mathbf{u} + \frac{\eta_p}{\Lambda}\nabla \cdot e^{\boldsymbol{\psi}} \\ \nabla \cdot \mathbf{u} = 0 \\ \frac{\partial \boldsymbol{\psi}}{\partial t} + (\mathbf{u}.\nabla)\boldsymbol{\psi} - (\mathbf{\Omega}.\boldsymbol{\psi} - \boldsymbol{\psi}.\mathbf{\Omega}) + 2\mathbf{B} = \frac{1}{\Lambda}\ (e^{-}\boldsymbol{\psi} - \mathbf{I}) \end{cases} \tag{19}$$

3 FINITE ELEMENT DISCRETIZATION

The choice of FEM spaces for the Stokes problem is subject to the well-known compatibility condition between the velocity and pressure spaces, the so-called $\inf - \sup$ condition named after Ladyzhenskaya, Babuška and Brezzi (LBB) [22]

$$\sup_{\mathbf{u}\in\mathbf{V}_h} \frac{\int_\Omega \operatorname{div} \mathbf{u}\, q\, dx}{\|\mathbf{u}\|_{1,\Omega}} \geq \alpha \|q\|_{0,\Omega} \quad \text{for all } q \in Q_h. \tag{20}$$

Similarly, the addition of the weak form of the constitutive equation imposes further compatibility constraints onto the choice of the approximations spaces of the triple velocity-pressure-stress [11],

$$\sup_{\boldsymbol{\sigma}\in\mathbf{W}_h} \frac{\int_\Omega \operatorname{div} \boldsymbol{\sigma}\, \mathbf{u}\, dx}{\|\boldsymbol{\sigma}\|_{0,\Omega}} \geq \gamma \|\mathbf{u}\|_{1,\Omega} \quad \text{for all } \mathbf{u} \in \mathbf{v}_h, \tag{21}$$

where α and γ are two mesh-independent constants, $\|\cdot\|_{1,\Omega}$ and $\|\cdot\|_{0,\Omega}$ are the standard H^1 and $L^2(\Omega)$ norms and $\mathbf{V}_h \times Q_h \times \mathbf{W}_h \subset (H^1(\Omega))^2 \times L^2_0(\Omega) \times (L^2(\Omega))^4$. Fortin and Pierre [21] have shown that in the absence of the viscous contribution, the standard Lagrangian interpolation needs to satisfy the following conditions:

1. The velocity interpolation must satisfy the usual LBB condition.
2. If the extra-stress tensor is approximated by a discontinuous FE space, the strain rate must be a member of this space

$$\mathbf{D} = \frac{1}{2}(\nabla \mathbf{u} + \nabla \mathbf{u}^{\mathrm{T}}) \in \mathbf{W}_h, \quad \text{for all} \quad \mathbf{u} \in \mathbf{V}_h. \tag{22}$$

3. If the extra-stress tensor is approximated by a continuous FE space, the number of internal nodes must be larger than the number nodes on the side of an element used for the velocity interpolation.

The second condition is easily satisfied using a discontinuous Galerkin approach, see [20]. The last condition is established, for instance see [34], if the basic nine-node element for the velocity is subdivided into 4×4 bilinear subelements for the stresses, or using the subcell discretization, see Belblidia et al. [7]. The main drawback of this method is its large computational cost. Baranger and Sandri [5] have shown that the last condition needs to be imposed only in the absence of the pure viscous contribution, which allows a much larger class of discretization schemes. The introduction of DEVSS, a larger selection of FE spaces, is possible, see for instance [3,19]. Bonito and Burman [10] have shown that inf-sup stability as well as stability for convection-dominated flows are obtained by adding a term penalizing the jump of the solution gradient over element faces. Indeed, to maintain the elliptic character of the momentum equation the jump term of the following form may be introduced, see [50, 51],

$$J_u = \sum_{\text{edge E}} \max(\gamma \eta h_E, \gamma^* h_E^2) \int_E [\nabla \mathbf{u}][\nabla \mathbf{v}] ds \tag{23}$$

which relaxes the choice of the stress space in the case of absence of pure viscous contribution. Nevertheless the convective terms of the constitutive equations may need further treatment, similarly further jump terms for the stress may be introduced:

$$J_\sigma = \sum_{\text{edge E}} \gamma h_E^2 \int_E [\nabla \boldsymbol{\sigma}][\nabla \boldsymbol{\chi}] ds \tag{24}$$

3.1 The velocity-pressure-stress triple approximations

Since a reliable accuracy of the numerical solution is besides the robustness and efficiency one of the main issues in solving the above set of equations, we

utilize the LBB-stable conforming finite element pair Q_2P_1 which is known to be one of the "best" (see [2], [24], the contributions according to [24] and in the proceeding [6]), that means most accurate and robust finite element pairs for highly viscous incompressible flow, particularly together with local grid refinement techniques via hanging nodes. So, we restrict our study to the triple $Q_2/P_1^{\text{disc}}/Q_2$

$$\mathbf{V}_h = \{\mathbf{v}_h \in (H_0^1(\Omega_h))^2, \quad \mathbf{v}_{h|T} \in (Q_2(T))^2 \ \ \forall T \in \mathcal{T}_h, \quad \mathbf{v}_h = 0 \ \ \text{on} \ \ \partial\Omega_h\},$$

$$Q_h = \{p_h \in L^2(\Omega_h), \quad p_{h|T} \in P_1(T) \ \ \forall T \in \mathcal{T}_h\},$$
$$\mathbf{W}_h = \{\boldsymbol{\sigma}_h \in (L^2(\Omega_h))^4, \quad \boldsymbol{\sigma}_{h|T} \in (Q_2(T))^4 \ \ \forall T \in \mathcal{T}_h\}$$

and consider for each $T \in \mathcal{T}_h$ the bilinear transformation $\psi_T : \hat{T} \to T$ to the unit square T. So, $Q_2(T)$ is defined by

$$Q_2(T) = \left\{q \circ \psi_T^{-1} : q \in \text{span} < 1, x, y, xy, x^2, y^2, x^2y, y^2x, x^2y^2 > \right\} \tag{25}$$

with nine local degrees of freedom located at the vertices, midpoints of the edges and in the center of the quadrilateral. The space $P_1(T)$ consists of linear functions defined by

$$P_1(T) = \left\{q \circ \psi_T^{-1} : q \in \text{span} < 1, x, y > \right\} \tag{26}$$

with the function value and both partial derivatives located in the center of the quadrilateral, as its three local degrees of freedom. The velocity-pressure inf-sup condition is satisfied (see [8]) as well as the velocity-stress inf-sup condition in the presence of a purely viscous contribution [5]. However, the combination of the bilinear transformation ψ with a linear function on the reference square $P_1(\hat{T})$ would imply that the basis on the reference square did not contain the full bilinear basis. So, the method can at most be first order accurate on general meshes (see [2, 8])

$$\|p - p_h\|_0 = O(h). \tag{27}$$

The standard remedy (see [2, 40, 47]) is to consider a local coordinate system (ξ, η) obtained by joining the midpoints of the opposing faces of T. Then, we set on each element T

$$P_1(T) := \text{span} < 1, \xi, \eta > . \tag{28}$$

For this case, the inf-sup condition is also satisfied and the second order approximation is recovered for the pressure as well as for the velocity gradient, see [8, 22]

$$\|p - p_h\|_0 = O(h^2) \ \ \text{and} \ \ \|\nabla u - \nabla u_h)\|_0 = O(h^2). \tag{29}$$

For a smooth solution, the approximation error for the velocity in the L_2-norm is of order $O(h^3)$ which can easily be demonstrated for prescribed polynomials or for smooth data on appropriate domains [8].

4 ITERATIVE SOLVERS

We apply implicit 2nd order time stepping methods to preserve the high accuracy and robustness in nonstationary flow simulations, for instance the Crank-Nicolson or Fractional-Step-θ scheme, which allow adaptive time stepping due to accuracy reasons only [46], but which do not depend on CFL-like restrictions. The Navier-Stokes equations are discretized in time as follows

$$\frac{\mathbf{u}^{n+1}-\mathbf{u}^n}{\Delta t}+$$

$$\theta\left[(\nabla\mathbf{u}^{n+1})\mathbf{u}^{n+1}-\frac{1}{\rho}(-\nabla p^{n+1}+2\eta_s\Delta\mathbf{u}^{n+1}+\frac{\eta_p}{\Lambda}\nabla\cdot e^{\boldsymbol{\psi}^{n+1}})\right] \tag{30}$$

$$+(1-\theta)\left[(\nabla\mathbf{u}^{n})\mathbf{u}^{n}-\frac{1}{\rho}(-\nabla p^{n}+2\eta_s\Delta\mathbf{u}^{n}+\frac{\eta_p}{\Lambda}\nabla\cdot e^{\boldsymbol{\psi}^{n}})\right]=0$$

$$\nabla\cdot\mathbf{u}^{n+1}=0 \tag{31}$$

where $\mathbf{u}^n\sim\mathbf{u}(t_n)$. The LCR equation is discretized in the same way so that

$$\frac{\boldsymbol{\psi}^{n+1}-\boldsymbol{\psi}^n}{\Delta t}+ \tag{32}$$

$$\theta\left[\mathbf{u}^{n+1}\cdot\nabla\boldsymbol{\psi}^{n+1}-(\boldsymbol{\Omega}(\mathbf{u}^{n+1}).\boldsymbol{\psi}^{n+1}-\boldsymbol{\psi}^{n+1}.\boldsymbol{\Omega}(\mathbf{u}^{n+1}))+2\mathbf{B}(\mathbf{u}^{n+1})-\frac{1}{\Lambda}\,(e^{-\boldsymbol{\psi}^{n+1}}-\mathbf{I})\right]$$

$$+(1-\theta)\left[\mathbf{u}^{n}\cdot\nabla\boldsymbol{\psi}^{n}-(\boldsymbol{\Omega}(\mathbf{u}^{n}).\boldsymbol{\psi}^{n}-\boldsymbol{\psi}^{n}.\boldsymbol{\Omega}(\mathbf{u}^{n}))+2\mathbf{B}(\mathbf{u}^{n})-\frac{1}{\Lambda}\,(e^{-\boldsymbol{\psi}^{n}}-\mathbf{I})\right]=0.$$

The divergence of the exponential operator in equation (30) is approximated by the divergence of the conformation tensor via eigenvalue decomposition, $\nabla\cdot e^{\boldsymbol{\psi}^n}=\nabla\cdot e^{\boldsymbol{\psi}(\boldsymbol{\tau}^n)}=\nabla\cdot\boldsymbol{\tau}^n$. By choosing $\theta=\frac{1}{2}$ we obtain the fully implicit Crank-Nicolson method with second order accuracy.

Next, in each time step we discretize the above equations (30, 31, 32) by means of the described mixed finite element approach. As mentioned before, we restrict our study to the triple $Q_2/P_1^{\text{disc}}/Q_2$. In discrete form those equations may be written as follows

$$\underbrace{\begin{pmatrix} A_{\mathbf{u}}(\mathbf{u}) & C\circ\exp & B \\ C^{\sim} & A_{\boldsymbol{\psi}}(\mathbf{u}) & 0 \\ B^T & 0 & 0 \end{pmatrix}}_{Nonlinear\ operator\ \mathcal{K}}\begin{pmatrix}\mathbf{u}\\ \boldsymbol{\psi}\\ p\end{pmatrix}=\begin{pmatrix}\text{rhs}_{\mathbf{u}}\\ \text{rhs}_{\boldsymbol{\psi}}\\ \text{rhs}_p\end{pmatrix} \tag{33}$$

with $A_{\mathbf{u}}(\mathbf{u})=M(\mathbf{u})+L(\mathbf{u})+N(\mathbf{u})$, $A_{\boldsymbol{\psi}}(\mathbf{u})=\frac{1}{\Lambda}\exp^{-1}+N(\mathbf{u})+G_0(\boldsymbol{\Omega})$. Here, $A_{\mathbf{u}}(\mathbf{u})$ consists of mass, diffusive, and convective operators, $A_{\boldsymbol{\psi}}(\mathbf{u})$ consists of the transformation, convection, and rotation operators.

The 'price' to be paid for the enhanced accuracy and robustness properties of such coupled approaches is the more expensive solution of the resulting coupled nonlinear discrete systems, either in each time step or in a direct stationary approach. While operator-splitting schemes, for instance classical projection or pressure correction methods, reduce the complete solution to a sequence of much easier scalar problems, the outer coupling of such subproblems towards the fully coupled solution is still a challenging problem, particularly if the elastic stress equation has to be taken into account or in the case of high Weissenberg numbers. The key problem in such approaches is the construction of optimal pressure Schur complement operators for updating the pressure which is even for the Navier-Stokes equations a challenge (see [30] for an overview). As an alternative, fully coupled monolithic solvers have proven to be competitive, as demonstrated in [35], [42], [45] for non-isothermal problems as well as in [24], [48], [49] for fluid-structure interaction problems.

First of all, the Newton iteration is applied to the global system of equation (33) with damping parameter, ω^l, which has to be determined such that certain error measures decrease (see [15], and for implementation see also [24], [47], [14]),

$$\mathbf{X}^{l+1} = \mathbf{X}^l + \omega^l \mathbf{J}^{-1}(\mathbf{X}^l)\mathbf{R}(\mathbf{X}^l) \tag{34}$$

with $\mathbf{X} = (\mathbf{u}_h, \boldsymbol{\psi}_h, p_h)$ in our setting, $\mathbf{J}(\mathbf{X}^l) = \left[\frac{\partial \mathbf{R}(\mathbf{X}^l)}{\partial \mathbf{X}}\right]$ is the Jacobian matrix, and $\mathbf{R}(\mathbf{X}^l) = \left(\text{def}_{\mathbf{u}}^l \ \text{def}_{\boldsymbol{\psi}}^l \ \text{def}_p^l\right)^T$ is the residual coming from the discrete problem of the system (33). This improves the chance of better convergence by adaptively changing the length of the correction factor, and thus, it ensures a monotone convergence. The updated solutions are computed through the Jacobian which is calculated via a divided difference approximation,

$$\left[\frac{\partial R(u^n)}{\partial u}\right]_{ij} \approx \frac{R_i(u^n + \epsilon e_j) - R_i(u^n - \epsilon e_j)}{2\epsilon} \tag{35}$$

where $e_j = \delta_{ij}$ is the standard Kronecker symbol. Another possibility is by calculating the Frechét-derivative at the continuous level, which however can be very complicated for complex nonlinear flow models, see [47], [43]. Finally, we deal with a linearized system of equations at each Newton iteration which is usually treated via Krylov-space methods (see [29], [39]). However, such Krylov-space methods, like for instance BiCGStab or GMRES, typically suffer from convergence problems since the numerical behaviour strongly depends on the mesh size. In contrast, we discuss special monolithic multigrid solvers which exploit the underlying hierarchical mesh structures such that a mesh-independent convergence behaviour can be obtained. Inside the multigrid solver, a restriction operator is applied to the residual after pre-smoothing on the actual mesh level and a direct linear solver is utilized to obtain the

coarsest grid solution. The applied smoother is of Vanka-type as in [14],

$$\begin{bmatrix} \mathbf{u}^{l+1} \\ \boldsymbol{\psi}^{l+1} \\ p^{l+1} \end{bmatrix} = \begin{bmatrix} \mathbf{u}^{l} \\ \boldsymbol{\psi}^{l} \\ p^{l} \end{bmatrix} + \omega^l \sum_{T \in \mathcal{T}_h} [\mathbf{J}]^{-1}_{|T} \begin{bmatrix} Res_{\mathbf{u}} \\ Res_{\boldsymbol{\psi}} \\ Res_p \end{bmatrix}_{|T} . \tag{36}$$

Prolongation is then applied which is followed by post-smoothing to give a better approximation. These steps continue until a V or F-cycle of multigrid iterations is finished. We use a fixed number of smoothing steps of the shown 'Vanka' smoother which acts locally in each element Ω_i on all levels. Here, the 'summation' over each element represents an assembling technique and the inverse of the local systems on each element Ω_i (in this case of size 48×48) is computed by a direct linear solver.

5 NUMERICAL SIMULATION

5.1 Driven cavity flow

We consider the numerical simulation of both directly steady and nonstationary flow in a lid-driven cavity for the Oldroyd-B model. The initial condition for the stress tensor is unity and a regularized velocity boundary condition is implemented such that $\mathbf{u}(\mathbf{x}, t) = (8(1+tanh\, 8(t-0.5))x^2(1-x)^2, 0)^T$ on the top boundary while zero velocity on the rest of boundary is prescribed. For direct steady simulations the velocity profile evolves to $\mathbf{u}(\mathbf{x}, t) = (16x^2(1-x)^2, 0)^T$ on the boundary. For the total viscosity (zero-shear viscosity), ν_s and ν_p are equal to 1. The simulation is performed with the mesh size $h = 1/64$ and with coarse mesh size $h = 1/4$. The time step is chosen to be $\Delta t = 0.1$ in the sense that no further improvement in kinetic energy with respect to smaller time steps could be observed. The number of cells for the corresponding computation level n is $\mathrm{L}n = 2^{4+2n}$. We calculate the kinetic energy by $\frac{1}{2}\int_\Omega \|\mathbf{u}_h\|_2^2 dx$ and analyze the impact of jump stabilization for different We numbers.

For We=1, the kinetic energy seems to reach a steady state as shown in Fig. 1 and it remains steady at least up to time $t = 30$. As the We number increases the kinetic energy oscillates stronger and the LCR variable becomes more spurious at time $t = 30$, see Fig. 2. Longer computation times may lead to numerical break down. EO-FEM in this case is able to relax these oscillations, thus it significantly improves numerical stability. In Fig. 3, streamline visualization is needed to demonstrate the behaviour of the flow inside of the domain. As in high inertia flow, we observe also a change of the streamline pat-

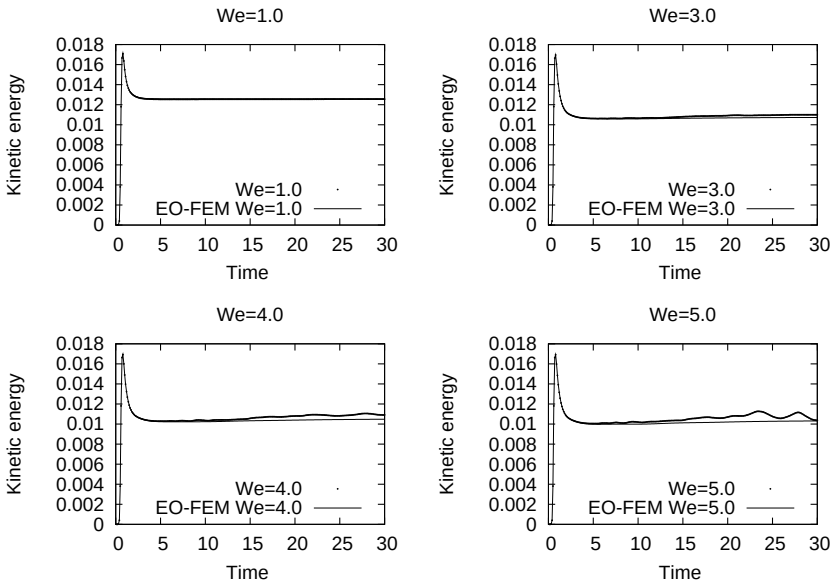

Fig. 1. Kinetic energy until $t = 30$ for different We numbers with and without EO-FEM.

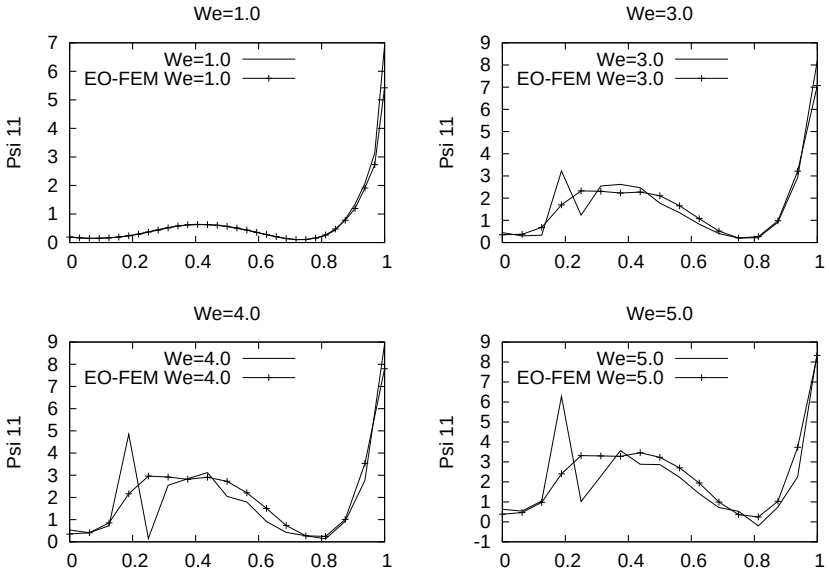

Fig. 2. Cutline of ψ_{11} at $x = 0.5$, $t = 30$, for different We numbers with and without EO-FEM.

terns as the We number increases. For this purpose, we simulate direct steady problems using a low We number as an initial solution and consecutively obtain solutions at higher We numbers. At lower We numbers the bottom corner vortex looks equally the same. But when the We number increases, the lower left vortex decreases while the right one evolves in size. Thus, it shifts the whole flow field to the left.

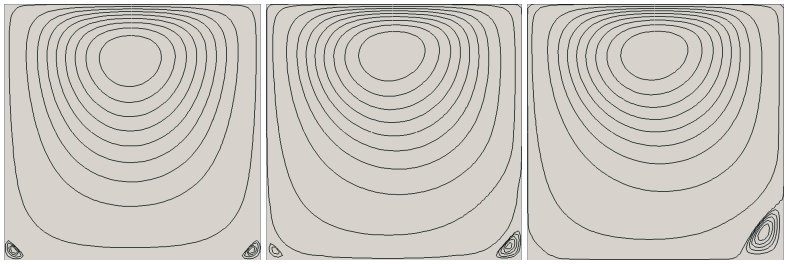

Fig. 3. Shape changing of corner vortex in a cavity flow. From left to right $We = 1, 3, 4$.

5.2 Planar flow around cylinder

Next, we consider planar flow around a cylinder where most numerical instabilities occur around Weissenberg number $We_{critical} = 0.7$. For $We < 0.7$ numerical instabilities do not occur or are less visible, and mesh convergence of normal stress can be obtained up to $We = 0.6$. Furthermore, mesh convergence of normal stress becomes also very clear at this stage as reported by many other studies [1, 12, 26]. Here, we try to simulate accurately by using local refinement near, around and in the wake of the cylinder. The full computational domain is symmetric so that it is reasonable to consider only half of it, at least for low We numbers. Fig. 4 shows the coarse mesh of the configuration with the position of local refinement. By local refinement we mean to refine for the next mesh level only those elements attached to the location that we prescribed before hand (bold line in Fig. 4). The refinement levels are denoted

Fig. 4. The coarse mesh for planar flow with a priori local refinement locations.

by R$ia$$j$ where i and j are the number of refinements. R$ia$$j$ means that firstly we do i times regular refinement and then j times local refinement. The difference between those meshes is the distribution of elements around the cylinder and in the wake, i.e. mesh R2a3 has the same number of elements around the cylinder and in the wake as mesh R5a0, but less total number of elements, see

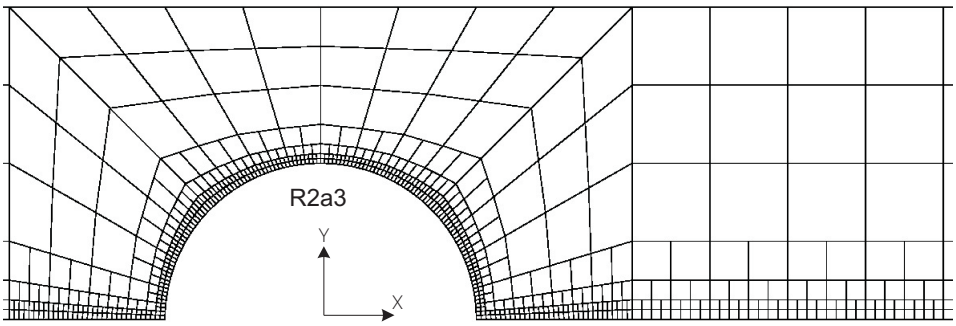

Fig. 5. Computational mesh R2a3 with local refinement.

Fig. 5 for an example. The inflow boundary profile for the stress variables (or ψ from LCR) must be calculated based on the inflow velocity boundary profile while the outflow stress boundary is set to natural ('Do nothing') boundary conditions [23]. The outflow velocity profile can be set either to Dirichlet (fully developed outflow) or natural boundary condition for which we tested both to see if there will be any effect for the results and to get rid of the question of how long should be the length of the downstream channel. We assume the flow to be fully developed at the inflow, and no-slip condition is applied on solid boundaries for the velocity. The above assumptions generate a stress profile at the inflow which can be analytically computed since the velocity profile is given at the inflow, see [16]:

$$\tau_{yy} = 1, \quad \tau_{xy} = \Lambda \frac{\mathrm{d}u_x}{\mathrm{d}y}, \quad \tau_{xx} = 1 + 2\left(\Lambda \frac{\mathrm{d}u_x}{\mathrm{d}y}\right)^2. \tag{37}$$

Next, we transform the stress boundary condition at the inflow into a boundary condition for the new variable $\boldsymbol{\psi}$ in LCR. At each point of the inflow boundary we calculate the stress components and transform them directly into $\boldsymbol{\psi}$ using their eigenvalues,

$$\lambda_{1,2} = \frac{1}{2}\left[tr\boldsymbol{\tau} \pm \sqrt{tr\boldsymbol{\tau}^2 - 4det\boldsymbol{\tau}}\right] \tag{38}$$

$$\boldsymbol{\psi} = \begin{pmatrix} c & s \\ -s & c \end{pmatrix} \begin{pmatrix} log\lambda_1 & 0 \\ 0 & log\lambda_2 \end{pmatrix} \begin{pmatrix} c & -s \\ s & c \end{pmatrix} \tag{39}$$

with the property $c^2 + s^2 = 1$. The direct steady computation for flow around cylinder starts by prescribing a velocity inflow profile, $u_x = 1.5(1 - \frac{y^2}{4})$. We collect results for three We numbers, $We = 0.6, 0.7, 0.8$, and plot the normal stress at the cylinder and in the wake. We show the results of stress convergence for several exemplary meshes for two different velocity outflow boundaries which can be summarized as follows: for different velocity outflow

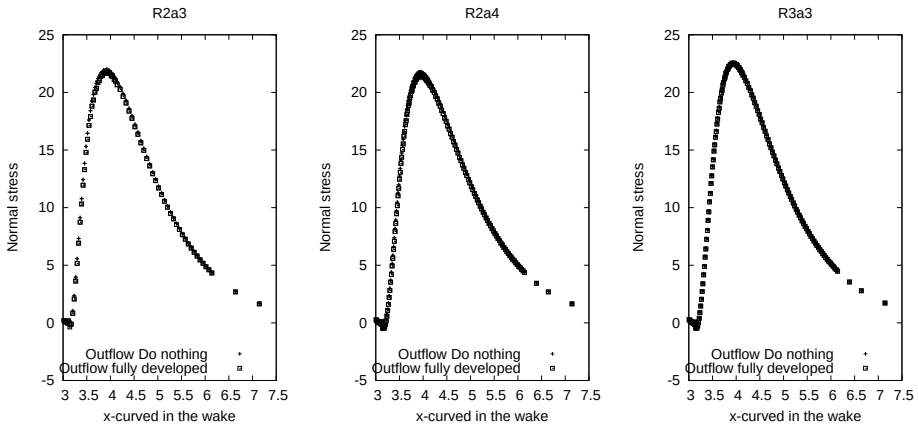

Fig. 6. Normal stress convergence with local refinement for two different velocity outflow conditions at $We = 0.7$.

boundaries, we observe no big difference or no difference at all when we set the velocity boundary condition to Dirichlet (fully developed flow) or 'Do nothing' condition [23], see Fig. 6. This means that the length of the downstream channel does not need to be very long in order to produce accurate result around the cylinder and in the wake, unless one wants to investigate more on what happens at the outflow which is in common not very important. Further re-

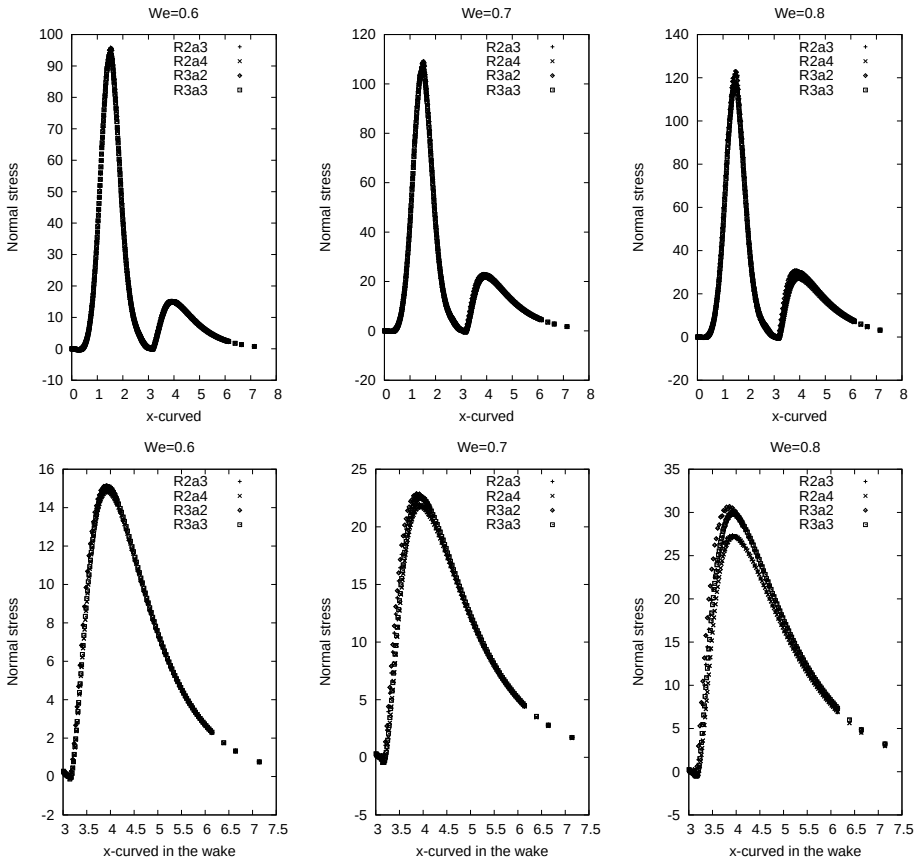

Fig. 7. Normal stress convergence with local refinement for three different We numbers. Bottom row: zoom of in the wake part

sults can be seen in Fig. 7 where for all three We numbers the stress converges for four different meshes. Only for $We = 0.8$ we notice a small difference in the wake between 2 regular refinements but this should be acceptable. The computation is in fact able to converge up to around $We = 1.8$ in which case the drag coefficients are comparable with different numerical techniques from other authors, see Fig. 8. Furthermore, we show again the influence of EO-FEM for which the drag coefficients are plotted against the We number for different levels, see Fig. 9. While usually the maximum We number, which can be obtained by LCR, is in the range of $We = 1.8$ or $We = 2.0$, see [1,26], here EO-FEM helps to go further as far as $We = 6.0$. Note that this is calculated with a direct steady approach which shows the big potential of EO-FEM stabilization for viscoelastic flow. As mentioned before, the linear subproblem is handled by a special monolithic multigrid solver. In Tab. 1 we show the multi-

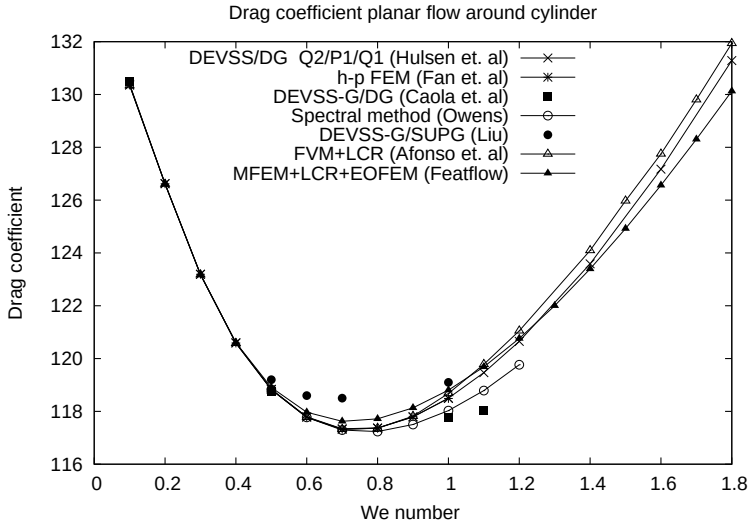

Fig. 8. Drag coefficient from different authors.

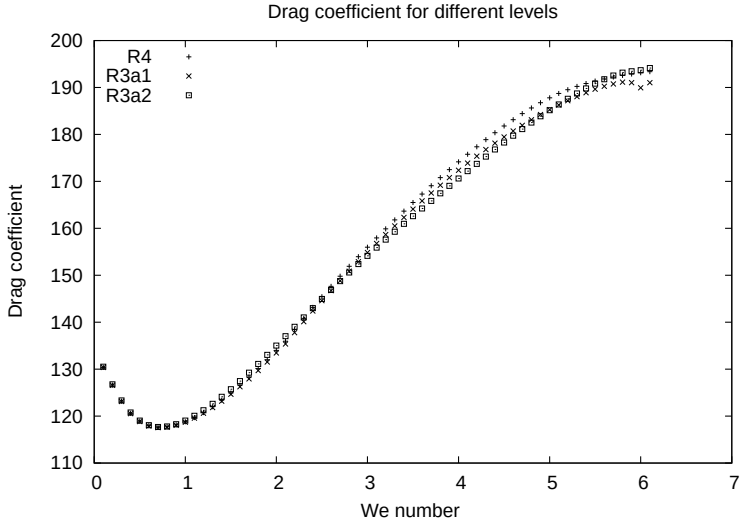

Fig. 9. Drag coefficient for different levels.

grid convergence in the direct steady approach with respect to the number of nonlinear iterations for increasing We numbers. Here, #NL/#LL denotes the number of nonlinear iterations versus the average number of linear iterations in each Newton step for nonlinear tolerance 10^{-5}. The number of smoothing step is 4 and the initial solution is the zero vector. The Newton-multigrid solver seems to be stable with respect to mesh refinement and to the nonlinearity of the problem as We number increases. More investigation on solver behaviour can be found in [13].

Table 1
Newton-multigrid behaviour

We	0.01		0.1		1.0	
Linear Tol	0.1	0.01	0.1	0.01	0.1	0.01
R1	9/2	5/3	10/1	7/3	14/1	10/3
R2	9/3	5/5	10/2	7/4	16/2	10/5
R3	9/3	5/6	10/3	7/5	16/2	11/5
R4	9/3	5/6	10/3	9/5	13/3	11/5

5.3 4 to 1 Contraction Problem

The 4:1 Contraction problem is one of the most well-known benchmarks for viscoelastic flow. The difficulties of this configuration are due to the sudden contraction from width 4 units to 1 unit, hence causing an extensional flow at the downstream channel. Similar to the planar flow around cylinder configuration, we prescribe Dirichlet data for velocity at the inflow which is parabolic and we set the outflow velocity to natural conditions [23] and no-slip condition at the solid walls. The stress inflow boundary is computed in the same way as before. The outflow and solid wall stress boundaries are set to natural boundary conditions. Here, we apply a priori local refinement around the corner to produce a smooth streamline for capturing the lip vortex as can be seen from Fig. 10 showing the coarse mesh. Our aim for this configuration is

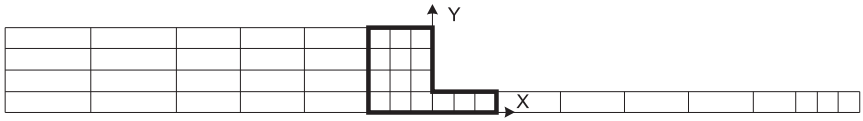

Fig. 10. Coarse mesh and local refinement location.

to describe the growth mechanism of the lip vortex as shown in experiments by Boger and Walter, see [9], where its enhancement at least depends on the type of contraction, the flow rate and the properties of the fluid. A coupled finite element approach with a Newton solver was presented for viscoelastic flow in [34] where they used a streamline-upwind method and found a weak salient corner in size. The lip vortex appears above $We = 2.0$ but disappears as the We number increases. Furthermore, in [32,33], streamline-upwind does not discover the lip vortex in the finite element context. In contrast to those, finite volume with a staggered grid approach has found the increasing lip vortex in size as We number increases, see [52]. Hence, lip vortex enhancement depends on the numerical techniques, the stabilization method and the mesh size. In this study, as already mentioned, we use the fully coupled approach

Fig. 11. Computational mesh for the contraction problem.

with consistent edge-oriented stabilization based on LCR for Oldroyd-B type of fluid. The mesh is shown in Fig. 11 where the distribution of elements is concentrated around the entrance corner utilizing hanging nodes. The lip vor-

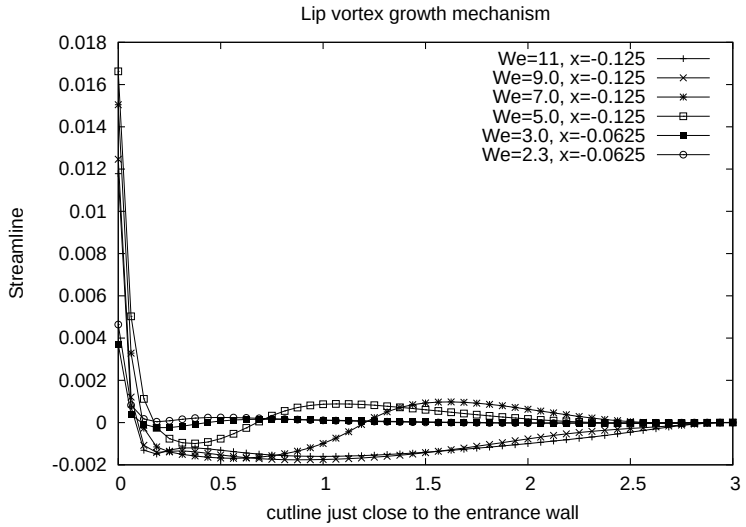

Fig. 12. Cutlines of streamfunction at $x = -0.0625$ and $x = -0.125$.

tex starts to appear at $We = 2.3$ which however is hardly visible in our case. Fig. 12 shows cutlines for the streamfunction close to the entrance wall where we can see the passage of the lip vortex as the cutline crosses the zero line for $We = 2.3$. Here, we take a line as close as possible to the wall in order to detect the first time appearance of the lip vortex as the We number increases. The width from the y-axis to this line can be taken as the smallest width of the cell close to the lip entrance which in our case corresponds to the width of the smallest element after refinement, $h = 0.0625$. As the lip vortex begins to grow, one may shift this line one cell width to the left in order to cross the

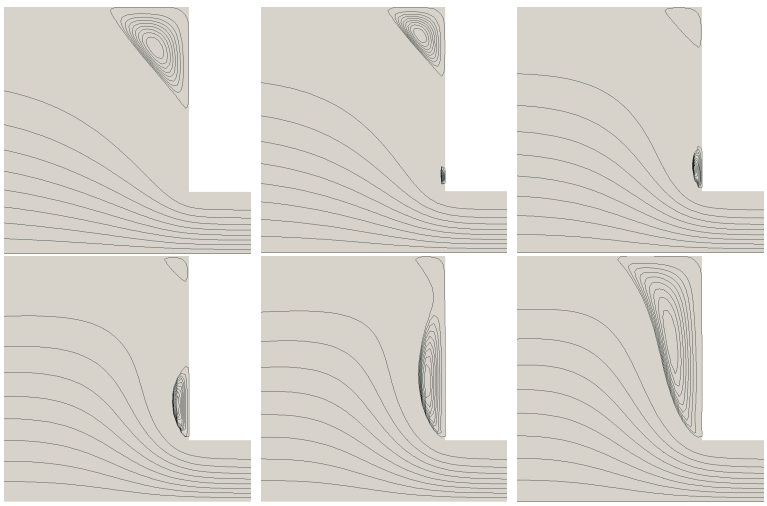

Fig. 13. The growth of lip vortex. First row: $We = 1.0, 3.0, 5.0$, second row: $We = 7.0, 9.0, 11.0$.

lower curvature of the streamfunction. Fig. 13 illustrates the appearance, the growth and the collision of the lip vortex and the salient corner vortex as the We number grows from $We = 1.0$ to $We = 11.0$ which is accompanied by a decreasing corner vortex. The appearance of the lip vortex, which is above $We = 2.0$, is in qualitatively good agreement with previous studies. Here, one can clearly see the streamline separation between the lip and the salient corner vortex before both vortices join together at $We = 9.0$ and form one big vortex at $We = 11.0$.

6 Summary

We have presented special numerical simulation techniques for viscoelastic flow within a monolithic finite element framework of utilizing the new LCR technique for Oldroyd-B type of fluids. Edge-oriented FEM stabilization is implemented to increase the numerical stability. Together with local refinement the method shows to be a very promising way for solving viscoelastic flow particularly for high We numbers. Several numerical examples of cavity flow, flow around cylinder and the growth of lip vortex in a contraction flow are also presented. Numerical stability has been significantly improved by the help of stabilization and mesh convergence for the stress variable can be achieved for several Weissenberg numbers in the flow around cylinder configuration. Future work should include the implementation of LCR in other viscoelastic models together with an additional coupling of the energy equation with a viscous dissipation term, see [14], in order to be able to simulate more realistic flow problems, particulary in 3D.

References

[1] Afonso, A., Oliveira, P. J., Pinho, F. T., and Alves, M. A. The log-conformation tensor approach in the finite-volume method framework. Journal of Non-Newtonian Fluid Mechanics, 157:55–65, 2009.

[2] Arnold, D.N., Boffi, D., and Falk, R.S. Approximation by Quadrilateral Finite Elements. Math. Comput., 71(239):909–922, 2002.

[3] Baaijens, F.P.T., Selen, S.H.A, Baaijens, H.P.W., and Meijer, H.E.H. Viscoelastic flow past a confined cylinder of a low density polyethylene melt. J. Non-Newtonian Fluid Mechanics, 68:173–203, 1997.

[4] Bajaj, M., Pasquali, M., and Prakash, J. R. Coil-stretch transition and the breakdown of computations for viscoelastic fluid flow around a confined cylinder. Journal of Rheology, 52:197–223, 2008.

[5] Baranger, J. and Sandri, D. Formulation of Stokes problem and the linear elasticity equations suggested by Oldroyd model for viscoelastic flow. Math. Modell. Numer. Anal, 26:231–345, 1992.

[6] Bathe, K., J., Editor. Computational Fluid and Solid Mechanics. Elsevier, 2001. Proceedings First MIT Conference on Computational Fluid and Solid Mechanics Vol. 2.

[7] Belblidia, F., Matallah, H., Puangkird, B., and Webster, M. F. Alternative subcell discretisations for viscoelastic flow: Stress interpolation. J. Non-Newtonian Fluid Mechanics, 146:59–78, 2007.

[8] Boffi, D. and Gastaldi, L. On the quadrilateral Q2-P1 element for the Stokes problem. Int. J. Numer. Meth. Fluids, 39:1001–1011, 2002.

[9] Boger, D. V. and Walters, K. Rheological Phenomena in Focus. Elsevier, 1993. Amsterdam.

[10] Bonito, A. and Burman, E. A continuous interior penalty method for viscoelastic flows. Siam Journal of Scientific Computing, 30:1156–1177, 2008. to appear.

[11] Brezzi, F. and Fortin, M. Mixed and Hybrid Finite Element methods. Springer, Berlin, 1986.

[12] Coronado, O. M., Arora, D., Behr, M., and Pasqualli, M. A simple method for simulating general viscoelastic fluid flows with an alternate log-conformation formulation. Journal of Non-Newtonian Fluid Mechanics, 147:189–199, 2007.

[13] Damanik, H. Numerical simulation of highly viscous non-isothermal viscoelastic fluids. Technische Universität Dortmund, 2010. PhD thesis.

[14] Damanik, H., Hron, J., Ouazzi, A., and Turek, S. A monolithic FEM–multigrid solver for non-isothermal incompressible flow on general meshes. Journal of Computational Physics, 228:3869–3881, 2009.

[15] Dennis, Jr., J. E. and Schnabel, R. B. Numerical Methods for Unconstrained Optimization and Nonlinear Equations. SIAM, 1996.

[16] Dou, H.-S. and Phan-Thien, N. The flow of an Oldroyd–B fluid past a cylinder in a channel: adaptive viscosity vorticity (davss-ω) formulation. Journal of Non-Newtonian Fluid Mechanics, 87:47–73, 1999.

[17] Fattal, R. and Kupferman, R. Constitutive laws for the matrix-logarithm of the conformation tensor. J. Non-Newton. Fluid Mech., 123:281–285, 2004.

[18] Fattal, R. and Kupferman, R. Time-dependent simulation of viscoelastic flows at high Weissenberg number using the log-conformation representation using matrix logarithms. J. Non-Newton. Fluid Mech., 126:23–37, 2005.

[19] Fortin, A. and Guénette, R.and Pierre R. On the Discrete EVSS Method. Comp. Methods Appl. Mech. Engrg., 189:121–139, 2000.

[20] Fortin, M. and Fortin, A. A new approach for the FEM simulation of viscoelastic flows. J. Non-Newtonian Fluid Mech, pages 295–310, 1989.

[21] Fortin, M. and Pierre, R. On the convergence of the mixed method of Crochet and Marchal for viscoelastic flows, Computer Methods in Applied. Mechanics and Engineering, 73:341–350, 1989.

[22] Girault, V. and Raviart, P. A. Finite Element Methods for Navier-Stokes equations. Springer, 1986. Berlin-Heidelberg.

[23] Heywood, J. G., Rannacher, R., and Turek, S. Artificial boundaries and flux and pressure conditions for the incompressible Navier-Stokes equations. International Journal for Numerical Methods in Fluids, 22:325–352, 1992.

[24] Hron, J. and Turek, S. A monolithic FEM/multigrid solver for ALE formulation of fluid structure interaction with application in biomechanics. In H.-J. Bungartz and M. Schäfer, editors, Fluid–Structure Interaction – Modelling, Simulation, Optimization, number 53 in Lecture Notes in Computational Science and Engineering, pages 146–170. Springer, Berlin, 2006. ISBN 3-540-34595-7 (Buch im LH vorhanden).

[25] Hulsen, M. A. A sufficient condition for a positive definite configuration tensor in differential models. Journal of Non-Newtonian Fluid Mechanics, 38:93–100, 1990.

[26] Hulsen, M. A., Fattal, R., and Kupferman, R. Flow of viscoelastic fluids past a cylinder at high Weissenberg number: Stabilized simulations using matrix logarithms. Journal of Non-Newtonian Fluid Mechanics, 127:27–39, 2005.

[27] Joseph, D. D. Fluid Dynamics of Viscoelastic Liquids. Springer, 1990. Applied Mathematical Sciences 84.

[28] Keunings, R. A survey of computational rheology. Proc. XIIIth Int. Congr. on Rheology, 1:7–14, 2000.

[29] Knoll, D. A. and Mousseau, V. A. On Newton-Krylov multigrid methods for the incompressible Navier-Stokes equations. Journal of Computational Physics, 163:262–267, 2000.

[30] Kuzmin, D., Löhner, R., and Turek, S. Flux–Corrected Transport. Scientific Computation. Springer, Berlin, 2005. Subtitle: Principles, Algorithms and Applications, ISBN 3-540-23730-5.

[31] Lee, Y.-J. and Xu, J. New formulations, positivity preserving discretizations and stability analysis for non-newtonian flow models. Computer methods in applied mechanics and engineering, 195:1180–1206, 2006.

[32] Luo, X.-L. and Tanner, R. I. A streamline element scheme for solving viscoelastic flow problems. part i. differential constitutive models. Journal of Non-Newtonian Fluid Mechanics, 21:179–199, 1986.

[33] Luo, X.-L. and Tanner, R. I. A streamline element scheme for solving viscoelastic flow problems. part ii. integral constitutive models. Journal of Non-Newtonian Fluid Mechanics, 22:61–89, 1986.

[34] Marchal, J.M. and Crochet, M.J. A new mixed finite element for calculating viscoelastic flow. J. Non-Newtonian. Fluid Mech, 26:77–114, 1987.

[35] McHugh, P. R. and Knoll, D. A. Fully coupled finite volume solutions of the incompressible Navier-Stokes and energy equations using an inexact Newton method. International Journal for Numerical Methods in Fluids, 19:439–455, 1994.

[36] Oldroyd, J. G. On the formulation of rheological equations of state. Proc. R. Soc. London, Ser. A 200, 523, 1950.

[37] Owens, R. G. and Phillips, T. N. Computational Rheology. Imperial College Press, 2002. London.

[38] Pan, T.-W. and Hao, J. Numerical simulation of a lid-driven cavity viscoelastic flow at high Weissenberg numbers. C. R. Acad. Sci. Paris, 344:283–286, 2007.

[39] Pernice, M. and Tocci, M. D. A multigrid-preconditioned Newton-Krylov method for the incompressible Navier-Stokes equations. SIAM J. Sci. Comput., 23:398–418, 2001.

[40] Rannacher, R. and Turek, S. A Simple nonconforming quadrilateral Stokes element. Numer. Methods Partial Differential Equations, 8:97–111, 1992.

[41] Renardy, M. A comment on smoothness of viscoelastic stresses. Journal of Non-Newtonian Fluid Mechanics, 138:204–205, 2006.

[42] Salinger, A. G., Lehoucq, R. B., Pawlowski, R. P., and Shadid, J. N. Computational bifurcation and stability studies of the 8x1 thermal cavity problem. Int. J. Num. Meth. Fluids, 40:1059–1073, 2002.

[43] Schmachtel, R. and Turek, S. Fully coupled and operator–splitting approaches for natural convection. International Journal for Numerical Methods in Fluids, 40:1109–1119, 2002.

[44] Schowalter, W. R. Mechanics of Non-Newtonian Fluids. Pergamon Press, 1978. Great Britain.

[45] Shadid, J. N., Salinger, A. G., Pawlowski, R. P., Lin, P. T., Hennigan, G. L., Tuminaro, R. S., and Lehoucq, R. B. Large-scale stabilized FE computational analysis of nonlinear steady-state transport/reaction systems. Comput. Methods Appl. Mech. Engrg., 195:1846–1871, 2006.

[46] Turek, S. A comparative study of time–stepping techniques for the incompressible Navier–Stokes equations: From fully implicit non–linear schemes to semi–implicit projection methods. International Journal for Numerical Methods in Fluids, 22:987–1011, 1996.

[47] Turek, S. Efficient solvers for incompressible flow problems: An algorithmic and computational approach. Springer, 1999. LNCSE 6.

[48] Turek, S. and Hron, J. A monolithic FEM solver for an ALE formulation of fluid–structure interaction with configuration for numerical benchmarking. In P. Wesseling, E. Onate, and J. Periaux, editors, Books of Abstracts European Conference on Computational Fluid Dynamics, page 176. nn, 2006. Eccomas CFD 2006.

[49] Turek, S. and Hron, J. Numerical techniques for multiphase flow with liquid–solid interaction. In G. P. Galdi, R. Rannacher, A. M. Robertson, and S. Turek, editors, Hemodynamical Flow Modeling, Analysis and Simulation, volume 37 of Oberwolfach Seminars, pages 379–501. Birkhäuser, 2008.

[50] Turek, S. and Ouazzi, A. Unified edge–oriented stabilization of nonconforming FEM for incompressible flow problems: Numerical investigations. J. Numer. Math., 15:299–322, 2007.

[51] Turek, S., Ouazzi, A., and Schmachtel, R. Multigrid Methods for Stabilized Nonconforming Finite Elements for Incompressible Flow involving the Deformation Tensor formulation. J. Numer. Math., 10:235–248, 2002.

[52] Yoo, J. Y. and Na, Y. A numerical study of the planar contraction flow of a viscoelastic fluid using the simpler algorithm. Journal of Non-Newtonian Fluid Mechanics, 30:89–106, 1991.